Monthly Notices
of the
ROYAL ASTRONOMICAL SOCIETY

MNRAS **468,** 1442–1452 (2017)
Advance Access publication 2017 March 7

doi:10.1093/mnras/stx559

Revisiting the extremely fast disc wind in a gravitationally lensed quasar APM 08279+5255

Kouichi Hagino,[1⋆] Chris Done,[1,2] Hirokazu Odaka,[3] Shin Watanabe[1,4] and Tadayuki Takahashi[1,4]

[1]*Institute of Space and Astronautical Science (ISAS), Japan Aerospace Exploration Agency (JAXA), 3-1-1 Yoshinodai, Chuo, Sagamihara, Kanagawa 252-5210, Japan*
[2]*Department of Physics, University of Durham, South Road, Durham DH1 3LE, UK*
[3]*KIPAC, Stanford University, 452 Lomita Mall, Stanford, CA 94305, USA*
[4]*Department of Physics, University of Tokyo, 7-3-1 Hongo, Bunkyo, Tokyo 113-0033, Japan*

Accepted 2017 March 2. Received 2017 March 1; in original form 2016 November 2

ABSTRACT

The gravitationally lensed quasar APM 08279+5255 has the fastest claimed wind from any active galactic nucleus, with velocities of 0.6–0.7c, requiring magnetic acceleration as special relativistic effects limit all radiatively driven winds to $v < 0.3$–$0.5c$. However, this extreme velocity derives from interpreting both the narrow and broad absorption features in the X-ray spectrum as iron absorption lines. The classic ultrafast outflow source PDS 456 also shows similar absorption systems, but here the higher energy, broader feature is generally interpreted as an absorption edge. We reanalyse all the spectra from APM 08279+5255 using a full 3D Monte Carlo radiative transfer disc wind model for the ionized wind at 0.1–0.2c, together with complex absorption from lower ionization material, and find that this is a better description of the data. Thus, there is no strong requirement for outflow velocities beyond 0.2c, which can be powered by radiation driving. We show that UV line driving is especially likely given the spectral energy distribution of this source which is intrinsically UV bright and X-ray weak. While the peak of this emission is unobservable, it must be luminous enough to power the observed hot dust, favouring at least moderate black hole spin.

Key words: black hole physics – radiative transfer – galaxies: active – galaxies: individual: APM 08279+5255 – X-rays: galaxies.

1 INTRODUCTION

Accretion disc winds from active galactic nuclei (AGN) are thought to play an important role in the evolution of the supermassive black holes and their host galaxies. Winds with a kinetic power which is only 5 per cent of the Eddington luminosity, $L_{\rm Edd}$, can quench star formation in the bulge by sweeping away the gas reservoir, and quantitatively reproduce the observed relation between the properties of the black hole and the galaxies (e.g. King 2010).

The most powerful winds in AGN have recently been revealed by X-ray observations showing ultrafast outflows (UFOs; e.g. Chartas et al. 2002; Reeves, O'Brien & Ward 2003; Pounds et al. 2003b,a; Tombesi et al. 2010; Gofford et al. 2013). These are seen as absorption lines of Fe XXV and/or Fe XXVI ions in the X-ray band, blueshifted by more than 10 000 km s^{-1} i.e. 0.03c (Tombesi et al. 2010). Such features were seen in up to 35 per cent of local AGN (Tombesi et al. 2010 but see Laha et al. 2014 and Tombesi & Cappi 2014). The most convincing have large column density of $\sim 10^{23}$ cm^{-2} and fast velocity of $\sim 0.1c$, where the associated kinetic power is estimated to be high enough to play a key role in the co-evolution of the black holes and galaxies.

In spite of its importance, the physical properties of UFOs are not fully understood. One of the major uncertainties is how the outflows are launched and accelerated. Continuum-driven winds require $L \gtrsim L_{\rm Edd}$, while many of the sources with detected (though sometimes controversial) UFOs have $L \sim 0.1 L_{\rm Edd}$ (e.g. IC 4329A, Mkn 509, Akn 120: Laha et al. 2014; Tombesi & Cappi 2014). UV line driving only works if the material has substantial UV opacity i.e. is not highly ionized. Strong X-ray illumination will overionize the material, and shielding the gas (e.g. Murray & Chiang 1998; Proga & Kallman 2004) is not easy as X-rays can scatter around the shield (Higginbottom et al. 2014). Thermal winds, driven by the pressure gradient of X-ray-heated gas, have much smaller velocities as they are launched at fairly large distances from the source, where material heated to the Compton temperature is unbound (Begelman,

⋆ E-mail: hagino@astro.isas.jaxa.jp

McKee & Shields 1983). This only leaves magnetic driving, which depends on the (unknown) field geometry, so no predictions are possible (Proga et al. 2000).

Without a physical mechanism, most current studies of UFOs have concentrated on constraining the physical properties of outflow. However, it is difficult to self-consistently model the emission and absorption from the UFOs since the wind geometry is probably not spherical (Elvis 2000; Proga & Kallman 2004; Risaliti & Elvis 2010). Such asymmetric geometries require Monte Carlo radiative transfer calculations to derive the emission and absorption self-consistently. Such simulations were performed by Sim et al. (2008, 2010a,b), but were used in detailed modelling of only two individual sources, PDS 456 (Reeves et al. 2014) and PG 1211+143 (Sim et al. 2010a).

In our previous work (Hagino et al. 2015), we developed a new 3D Monte Carlo simulation code for accretion disc winds in order to match to observational data from UFOs. Our code can calculate radiative transfer in H- and He-like ions in a realistic accretion disc wind geometry. We applied this simulation to all the *Suzaku* spectra of PDS 456, and successfully reproduced the changing UFO properties seen in this source by moderate changes in the velocity (0.2–0.3c) and the angle to the line of sight of a disc wind. However, the main new aspect of this paper was that it re-assessed the possibility that the outflow was a UV line driven disc wind as this object has $L \sim L_{\rm Edd}$, with a spectral energy distribution (SED) which peaks in the UV and is X-ray weak. A more favourable set of circumstances for UV line driving (helped by radiation pressure as $L \sim L_{\rm Edd}$) is hard to imagine. The outflow velocity is also characteristic of UV line driven disc winds (Proga & Kallman 2004; Risaliti & Elvis 2010; Nomura et al. 2013, 2016), as is the fluctuation behaviour about a steady state structure (Proga & Kallman 2004). The observed ionization state is far too high for UV line driving, but the acceleration could take place in much lower ionization material close to the disc, which becomes ionized and enters the line of sight only when it has lifted high enough to be ionized by illumination from the hotter inner disc and X-ray source (Hagino et al. 2015).

Our wind model was also applied to a putative broad iron line feature in 1H 0707-495 (Hagino et al. 2016). The characteristic sharp drop at ∼7 keV in the X-ray spectra of this source had been interpreted as the blue end of an extremely smeared disc reflection spectrum, requiring maximal black hole spin and a very low height of the point-like corona. Instead, our wind model successfully reproduced all the *XMM–Newton* observations of 1H 0707-495 (and the *NuSTAR* data) without any constrains on black hole spin, for a wind velocity of $v = 0.2c$ and a mass outflow rate of $\dot{M}_{\rm wind}/\dot{M}_{\rm Edd} = 0.2$. Interestingly, a closer look at the fit residuals suggest that the P Cygni iron emission line from the wind underpredicts the observed iron-K line emission. This could indicate that the wind has a larger opening angle than the model assumption of $\Omega/2\pi = 0.15$, as expected from a highly super-Eddington source (Done & Jin 2016).

However, neither UV line driving nor continuum radiation driving can launch a wind with an outflow of velocity $v \sim 0.7c$ found in a gravitationally lensed quasar APM 08279+5255 (Chartas et al. 2002; Saez, Chartas & Brandt 2009; Chartas et al. 2009; Saez & Chartas 2011) since radiative driving can accelerate only up to ∼0.3–0.4c due to radiation drag effects (Takahashi & Ohsuga 2015). Thus, this fast wind is evidence for a magnetic driving mechanism (Fukumura et al. 2010). This source is a high-redshift ($z = 3.91$) quasar, so that blueshifted H/He-like Fe lines are seen at ∼2 keV. At such an energy, the sensitivities of current instruments are much better than at 7–8 keV, where the absorption lines of UFOs at low redshift are observed. This enables the UFO signatures to be detected even though the X-ray flux is roughly one order of magnitude lower than PDS 456.

In this paper, we use our Monte Carlo wind code to fit the multi-epoch X-ray data from APM 08279+5255, to critically reassess whether the extremely fast velocities are required. We find we get good fits with a wind at 0.1–0.2c. We reassess the launch mechanism for the wind from the broad-band spectra energy distribution. While the overall Eddington fraction of the accretion flow is poorly constrained due to uncertainties in the magnification from lensing, the shape is UV bright and X-ray weak, favouring UV line driving. We assume a standard cosmology with $H_0 = 71\ {\rm km\ s^{-1}\ Mpc^{-1}}$, $\Omega_{\rm m} = 0.27$ and $\Omega_\Lambda = 0.73$, so that the redshift of the target $z = 3.91$ corresponds to the luminosity distance of $d_{\rm L} = 35.5$ Gpc and co-moving distance of 7.2 Gpc.

2 OBSERVATIONAL DATA AND COMPARISON WITH THE OTHER STRONG WIND SOURCES

APM 08279+5255 has been observed by *Chandra*, *XMM–Newton* and *Suzaku* as listed in Table 1. We use the same naming convention of Chartas et al. (2009) and Saez & Chartas (2011) except for the first *XMM–Newton* observation, which was not included in their analysis due to its short exposure time. We refer to this data as Epoch 0.

We processed EPIC-pn and -MOS data and removed dead and hot pixels by using SAS tasks EPPROC and EMPROC (SAS v.13.5.0), respectively. Time intervals when background rates of PATTERN = 0 events at energy >10 keV are higher than 0.35 counts s^{-1} for MOS and 0.4 counts s^{-1} for pn camera were removed. Only events with PATTERN ≤ 12 for MOS and PATTERN ≤ 4 for pn were considered in the spectral analysis. The total net exposure times are listed in Table 1. Spectra were extracted from circular regions of 64 arcsec diameter, while background spectra were extracted from circular regions of the same diameter for pn and annular regions from 100 to 300 arcsec diameter for MOS in the same chip as the source regions. We generated the corresponding response matrix and auxiliary response files by utilizing RMFGEN and ARFGEN.

Chandra data were reprocessed and extracted using the CIAO tools CHANDRA_REPRO and SPECEXTRACT. Spectra were extracted from circular regions of 4 arcmin diameter, while background spectra were extracted from annular regions from 6 to 30 arcmin diameter. The spectra were then grouped to obtain a minimum 40 counts in each bin.

We reduced the *Suzaku* XIS data with standard screening conditions: grade 0, 2, 3, 4 and 6 events were used. Data within 436 s of passage through the South Atlantic Anomaly, and within an Earth

Table 1. *XMM–Newton*, *Chandra* and *Suzaku* observations of APM 08279+5255.

Name	Observatory	Obs ID	Start Date	Net exposure (ks)[a]
Epoch 0	*XMM–Newton*	0092800101	2001-10-30	16.7/16.7/12.3
Epoch 1	*Chandra*	2979	2002-02-24	88.8
Epoch 2	*XMM–Newton*	0092800201	2002-04-28	76.4/77.2/63.2
OBS1	*Suzaku*	701057010	2006-10-12	102.3/102.3
OBS2	*Suzaku*	701057020	2006-11-01	102.3/102.3
OBS3	*Suzaku*	701057030	2007-03-24	117.1/117.2
Epoch 3	*XMM–Newton*	0502220201	2007-10-06	68.0/68.6/39.3
Epoch 4	*XMM–Newton*	0502220301	2007-10-22	75.8/75.8/57.9
Epoch 5	*Chandra*	7684	2008-01-14	88.1

Note. [a]Net exposure time of MOS1/MOS2/PN for *XMM–Newton*, ACIS for *Chandra* and FI/BI for *Suzaku*, respectively.

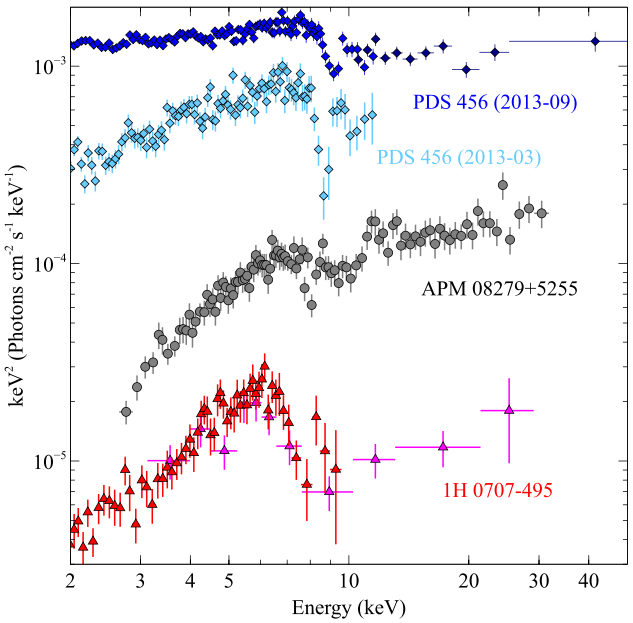

Figure 1. Comparison between the spectra of PDS 456 (blue/dark blue/cyan), 1H 0707-495 (red/magenta) and APM 08279+5255 (grey: Epoch 1). We show two spectra of PDS 456, one from 2013-09 where there is simultaneous *XMM–Newton-NuSTAR* data, and one from *Suzaku* in 2013-03 where the absorption line is strongest. The *XMM–Newton-NuSTAR* data of 1H 0707-495 are not simultaneous, but they are well matched. All spectra are shown in the rest frame, and 1H 0707-495 is scaled down by a factor of 10 for plotting purposes. All spectra show a narrow absorption line, and the one in APM 08279+5255 is less blueshifted than that in PDS 456. All spectra also show evidence for a broader absorption feature at higher energies, ∼10 keV. It is this feature in APM 08279+5255 which is the evidence for a 0.6c wind, yet in PDS 456 and 1H 0707-495 this feature is instead interpreted as mainly a photoelectric absorption edge from cool clumps embedded in the wind which also give rise to the hard 2–6 keV spectrum.

elevation angle <5° and Earth daytime elevation angles <20° were excluded. Spectra were extracted from circular regions of 2.9 arcmin diameter, while background spectra were extracted from annular region from 7.0 to 14.0 arcmin diameter.

Fig. 1 shows the strongest absorption line spectrum of APM 08279+5255 (grey, 2002 *Chandra* data), compared with the strongest absorption line states of PDS 456 (cyan, *Suzaku* 2013-03, ObsID: 707035030) and 1H 0707-495 (red, *XMM–Newton* 2011, ObsID: 0554710801). All the spectra are plotted in the rest frame so the APM 08279+5255 data extend up to 30 keV. Hence, we also extend the 1H 0707-495 and PDS 456 data to higher energies by including *NuSTAR* data. For PDS 456, we additionally plot the simultaneous *XMM–Newton* (blue, ObsID: 0721010401) and *NuSTAR* (dark blue, ObsID: 60002032006) spectra in 2013-09 (Nardini et al. 2015; Matzeu et al. 2016). However, for 1H 0707-495, there is no simultaneous observations of *XMM–Newton* and *NuSTAR*. None the less, we plot the *NuSTAR* data (magenta, 60001102004) as it matches well to the *XMM–Newton* data in both flux and spectral shape (Kara et al. 2015).

The spectra of these sources show very similar features in both continuum and lines. There is a fairly clear, relatively narrow absorption line, and then a broader absorption feature at higher energies in all the spectra. In PDS 456 and 1H 0707-495, these absorption features are strongest when the 2–5 keV continuum is hardest (Hagino et al. 2015, 2016; Matzeu et al. 2016), and the spectrum of APM 08279+5255 is similarly hard. It is clear that the narrow absorption lines in APM 08279+5255 are *less* blueshifted than in PDS 456 ($v \sim 0.3c$), making it unlikely that the wind is faster in APM 08279+5255 than in PDS 456.

The requirement for extreme velocity in APM 08279+5255 (0.40c for the grey spectra shown in Fig. 1) comes instead from the broad component of the absorption. Interpreting this as due to the Fe Kα line requires material with a large velocity spread, as well as material with a smaller spread to produce the narrower components of the line absorption (Chartas et al. 2009; Saez & Chartas 2011). However, as discussed by these authors, there is an alternative model, where the broad absorption is from bound-free edges. They showed that the edges predicted by the same highly ionized material as gives rise to the line is not completely sufficient to explain the data. However, in PDS 456, the broad absorption feature is generally interpreted as a complex absorption edge, with some contribution from the highly ionized wind material but with the majority produced in lower ionization material which is required to explain the continuum absorption at lower energies (Hagino et al. 2015; Matzeu et al. 2016). It is clear that APM 08279+5255 is more absorbed at low energies than even the most absorbed spectrum of PDS 456, so it is feasible that it has stronger edges, producing broad absorption up to ∼12 keV in these data. The narrow line component is blueshifted to ∼7.8 keV, so requires velocities of ∼0.15c, but here we explore whether the broader absorption structure at higher energies requires an additional faster wind or whether they can be produced in the same absorption structure which gives the hard spectrum below 5 keV.

3 MONTE CARLO SIMULATIONS OF THE WIND

3.1 Code overview

Our simulation code performs a radiative transfer calculation in a realistic wind geometry with a Monte Carlo method using MONACO (Odaka et al. 2011). MONACO is a general-purpose code for calculating the X-ray spectra from many astrophysical objects by tracking photon propagation and interaction with matter. The interaction position is determined by randomly drawing from an exponential distribution with a mean free path of the interactions, then the photon is absorbed or re-emitted according to the cross-sections of the interactions.

The physical processes in highly photoionized plasma are already implemented in the MONACO (see Watanabe et al. 2006). Photoionization, photoexcitation, radiative recombination, de-excitation and Compton scattering by free electrons are taken into account. As with the previous work (Hagino et al. 2015, 2016), only H- and He-like ions of Fe and Ni are considered in this work, which is reasonable assumption for the highly ionized winds like UFOs.

The ionization structure in the accretion disc wind is calculated by sequentially running XSTAR (Kallman et al. 2004), and then fixed during the radiative transfer calculation with MONACO. Ideally, the radiative transfer simulation and the ionization structure calculation should be calculated iteratively. However, it is not realistic to repeat the time-consuming Monte Carlo simulations many times, so that this simplified procedure is adopted.

We use a biconical geometry, which is often used for studying the radiative transfer in the accretion disc wind (Shlosman & Vitello 1993; Knigge, Woods & Drew 1995; Sim et al. 2008, 2010a). This geometry is described by three parameters: the solid angle Ω (or the covering factor $\Omega/4\pi$), the minimum radius $R_{\rm min}$ and the inner angle $\theta_{\rm min}$. The radial velocity follows an extension of the

Table 2. Assumed parameters for the simulations.

Parameter	Value
Acceleration index β	1.0
Turbulent velocity v_t	1000 km s^{-1}
Initial velocity v_0 ($=v_t$)	1000 km s^{-1}
Covering fraction $\Omega/4\pi$	0.15
Minimum radius R_{min}	$\simeq 2/(v_\infty/c)^2 R_g$
Inner angle θ_{min}	45°

CAK velocity law (Castor, Abbott & Klein 1975), parametrized by the initial velocity v_0, the terminal velocity v_∞ and the acceleration index β. The rotational velocity and the density are determined by conservation of angular momentum and mass, respectively. Assumed parameter values are listed in Table 2.

This wind model consists of only highly ionized material, whose typical ionization state is $\log \xi \sim 5$, consistent with our implementation, where only H- and He-like ions of Fe and Ni are considered. However, the observed spectra often show strong continuum absorption at lower energies as shown in Fig. 1. Such strong absorption requires much lower ionization material, which are not included in our wind model. For these, we additionally use a partially ionized absorber, which partially covers the source.

3.2 Parameters for APM 08279+5255

Our wind model is self-similar in ionization structure and column density for systems at different mass but the same Eddington ratio, so L_{bol}/L_{Edd} is the most important parameters for our wind model (Hagino et al. 2016). However, the intrinsic Eddington ratio of APM 08279+5255 is not clear as there is a large uncertainty in the magnification factor μ from gravitational lensing. Some papers report strong magnification with $\mu \sim 100$ (Egami et al. 2000; Krips et al. 2007; Weiß et al. 2007), but others claim much smaller values of $\mu \sim 2$–10 (Lewis et al. 2002; Solomon & Vanden Bout 2005; Riechers et al. 2009). Saez et al. (2009) circumvented this uncertainty by using instead the relation between the Eddington ratio, L_{bol}/L_{Edd} and X-ray photon index, Γ (Wang, Watarai & Mineshige 2004; Shemmer et al. 2006, 2008). According to this relation, they estimated the Eddington ratio to be $L_{bol}/L_{Edd} \simeq 0.2$–0.3 from the X-ray photon index of this source $\Gamma \sim 2.0$.

However, Fig. 1 shows that it is at least feasible that the spectrum of APM 08279+5255 is affected by absorption up to ∼20–30 keV so that Γ and hence L_{bol}/L_{Edd} are underestimated. We evaluate the intrinsic photon index by fitting the 5–8 keV spectra of all the observations. This energy range corresponds to ∼25–40 keV in the rest frame, where the continuum spectrum should be mostly free from absorption. The photon index is tied across all the observations, but the normalization is allowed to be free. All the normalizations are consistent with each other except for Epoch 4, where the flux is significantly higher than the other observations. This fit gives a photon index $\Gamma = 2.26^{+0.28}_{-0.27}$, corresponding to $L_{bol}/L_{Edd} \sim 0.5$ based on the relation in Grupe et al. (2010). This is a lower limit as any residual absorption means that the intrinsic X-ray photon index is larger. Therefore, the Eddington ratio in this source is $L_{bol}/L_{Edd} \gtrsim 0.5$, similar to that of PDS 456, so we use the same wind model for APM 08279+5255 as for PDS 456 (Hagino et al. 2015). This has parameters detailed in Table 2.

The change in depth of the absorption lines in PDS 456 and 1H 0707-495 from the hot wind can be reproduced by a changing viewing angle θ_{incl} (Hagino et al. 2015, 2016). As described in detail in Hagino et al. (2016), the energy of the absorption line depends on both the terminal wind speed and the viewing angle, whereas the width of the absorption line depends on the spread of velocities along the line of sight. Along the top edge of the bicone, the line width is fairly small and the blueshift indicates the true wind velocity since most of the wind is at its terminal velocity. On the other hand, at higher viewing angles, the absorption line is wider and the total blueshift is not so large since the line of sight cuts across the acceleration region, where the velocity is much lower. Thus, changing only the viewing angle gives very different observational properties of the absorption line for the same wind model. Fig. 2 shows quantitative results for the wind model used here in terms of the iron Kα line equivalent width, intrinsic width and velocity shift as a function of inclination angle. The equivalent width is the sum of both H and He-like Kα lines, as these merge together

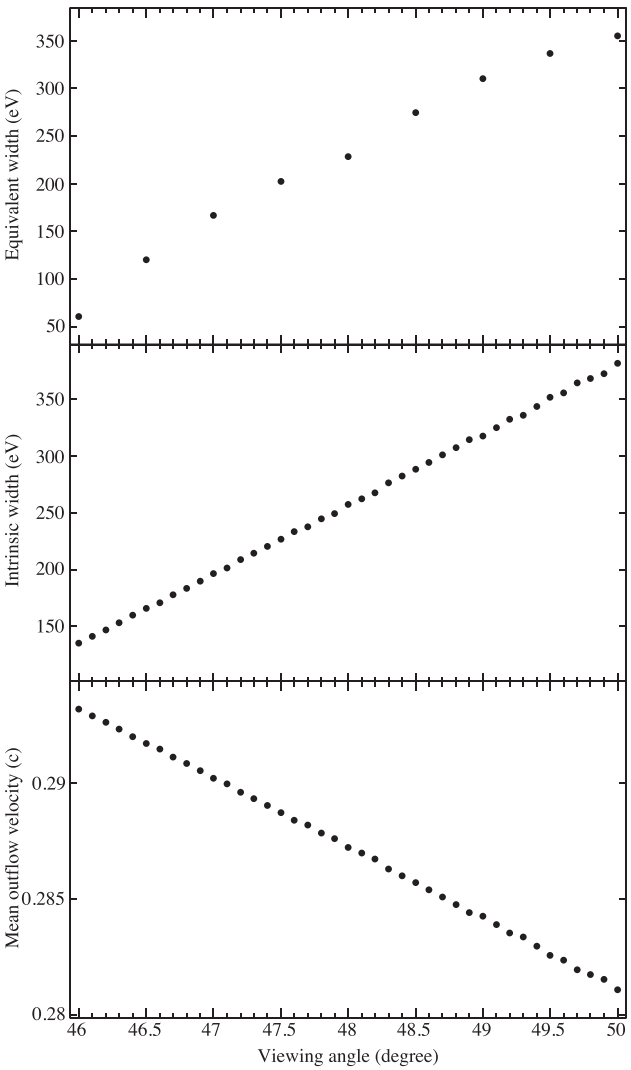

Figure 2. Equivalent width (top panel), intrinsic width (middle panel) and mean outflow velocity (bottom panel) of the blueshifted Fe XXV/Fe XXVI absorption lines as a function of viewing angle of the wind. The intrinsic width is defined as the full width at zero intensity, which corresponds to the energy difference between the fastest and slowest components of material along the line of sight. The equivalent widths of Fe XXV and Fe XXVI are co-added in this plot.

Table 3. Fitting parameters for Epoch 1.

		ZXIPCF*WIND*POWERLAW	ZPHABS*WIND*POWERLAW	ZPHABS*ZXIPCF*WIND*POWERLAW
Cold absorber[a]	$N_{\rm H}$ (10^{22} cm^{-2})	–	$6.2^{+0.8}_{-0.7}$	$6.5^{+1.4}_{-3.0}$
Cool clump	$v_{\rm out}$[b] (c)	$-0.09^{+0.32}_{-0.15}$	–	$0.19^{+0.07}_{-0.16}$
	$N_{\rm H}$ (10^{22} cm^{-2})	$2.9^{+8.1}_{-0.8}$	–	42^{+67}_{-41}
	$\log \xi$	<0.1	–	$1.6^{+2.8}_{-1.3}$
	$f_{\rm cov}$	>0.91	–	$0.51^{+0.22}_{-0.16}$
Hot wind	$v_{\rm out}$ (c)	$0.17^{+0.01}_{-0.01}$	$0.17^{+0.02}_{-0.02}$	$0.17^{+0.01}_{-0.02}$
	$\theta_{\rm incl}$ (°)	$48.6^{+1.3}_{-1.0}$	$47.8^{+1.1}_{-1.0}$	$48.2^{+1.3}_{-1.8}$
Power law	Γ	$1.64^{+0.07}_{-0.06}$	$1.63^{+0.06}_{-0.06}$	$1.92^{+0.22}_{-0.29}$
	Norm. (10^{-4})	$1.0^{+0.1}_{-0.1}$	$0.95^{+0.08}_{-0.07}$	$1.8^{+1.7}_{-0.8}$
Fit statistics	χ^2_ν	79.73/101	79.42/104	76.00/100
	Null Prob.	0.94	0.97	0.96

Notes. [a]Model for the cool clumps consists of ZXIPCF and CABS.
[b]Minus sign means the inflow/redshift.

for inclinations greater than 48°, whereas the intrinsic width and velocity shift are calculated for a single line.

In this work, we use the spectral model created for PDS 456 because its Eddington ratio is similar to APM 08279+5255. It is simulated for a wind with a mass outflow rate of $\dot{M}_{\rm wind}/\dot{M}_{\rm Edd} = 0.13$, a wind terminal velocity of $0.3c$, an ionizing photon spectrum with $L_{2-10{\rm keV}}/L_{\rm Edd} = 1.6 \times 10^{-3}$ and $\Gamma = 2.5$. This is implemented as a multiplicative model in XSPEC so it can approximately describe the effect of disc wind on any similar continuum, and we similarly incorporate any small change in velocity with a free redshift factor.

4 COMPARISON OF THE MONTE CARLO SIMULATIONS AND THE OBSERVED SPECTRA

4.1 Comparison with the Epoch 1 spectrum

We first do a detailed fit to the spectrum of Epoch 1 as this has the highest signal-to-noise absorption line detection. Similarly to PDS 456 and 1H 0707-495, the continuum absorption is modelled with absorption from partially ionized material that partially covers the source (ZXIPCF). This partially ionized absorber is required to reproduce the strong continuum absorption at low energies in the observed spectra which cannot be reproduced by our hot wind model. We additionally include the CABS model because the high-energy continuum should be suppressed by Compton scattering which is not included in ZXIPCF. We assume that CABS also partially covers the source with a same covering factor as ZXIPCF.

The partially ionized absorber is less ionized ($\log \xi < 0.1$) and covers more of the source ($f > 0.91$) than in PDS 456 and 1H 0707-495. Full parameters are listed in the left column of Table 3. The outflow velocity of the absorber is poorly constrained but is consistent with zero ($v = -0.24c$–$0.23c$). We assume it is at rest, and use the full covering neutral absorber ZPHABS instead of ZXIPCF. This model provides a similar χ^2 but has three fewer parameters as listed in the centre column of Table 3. In both models, the outflow velocity of the hot wind is similar to the local fast wind sources (Tombesi et al. 2010; Gofford et al. 2013), $0.18 \pm 0.02c$, and photon index of the intrinsic power law is very hard value of ∼1.6. Thus, the sharp downturn below 4 keV (which is not present in PDS 456 or 1H 0707-495, see Fig. 1) could be from an additional neutral screen of material. Hence, we add again a partially ionized absorber in order to investigate the effect of cool clumps in the wind. These were required in our previous studies and are also naturally expected to exist in hot winds due to the ionization instability (Krolik, McKee & Tarter 1981) or/and the Rayleigh–Taylor instability (Takeuchi, Ohsuga & Mineshige 2014). The best-fitting parameters are listed in the last column of Table 3, and the observed spectrum and model are shown in Fig. 3. Although adding cool clumps does not improve the fit significantly (F-test probability ∼30 per cent), this gives an interesting result. The outflowing velocity of the partially ionized absorber is consistent with the hot wind velocity. A similar result is found in PDS 456 (Matzeu et al. 2016), and it is consistent with our interpretation that the partially ionized absorber is due to cool clumps embedded in the hot phase of the wind. In this model, the absorption line at ∼8 keV is mainly set by the hot wind, the feature at ∼9 keV and the 4–6 keV continuum shape are mainly set by the partially ionized absorption, while the continuum below 4 keV is set by the neutral absorption. Adding the partially ionized absorber does not change the parameters of the neutral absorber or the hot wind, but the power-law continuum becomes steeper.

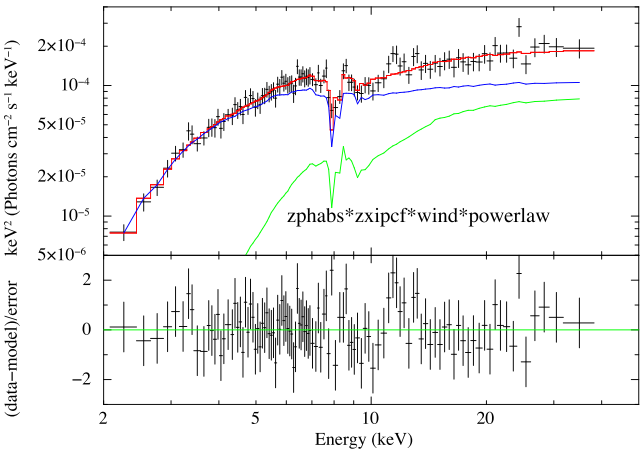

Figure 3. Observed spectrum and best-fitting model for Epoch 1. The absorbed component, unabsorbed component and sum of these components are plotted in green, blue and red, respectively.

Table 4. Fitting parameters for all the *XMM–Newton* and *Chandra* observations.

		Epoch 0	Epoch 1	Epoch 2	Epoch 3	Epoch 4	Epoch 5
Cold absorber	$N_{\rm H}$ (10^{22} cm^{-2})	$5.9^{+0.8}_{-1.5}$	$6.4^{+1.4}_{-4.6}$	$5.4^{+0.9}_{-0.9}$	$5.5^{+0.7}_{-0.7}$	$5.2^{+0.5}_{-0.5}$	$5.6^{+1.2}_{-1.1}$
Cool clump	$v_{\rm out}$ (c)	Tied to hot wind					
	$N_{\rm H}$ (10^{22} cm^{-2})	87^{+208}_{-67}	44^{+60}_{-42}	87^{+43}_{-38}	>254	138^{+163}_{-42}	76^{+159}_{-47}
	$\log \xi$	<2.9	$1.9^{+2.0}_{-2.0}$	$2.3^{+0.7}_{-0.3}$	$2.8^{+0.2}_{-1.4}$	$2.9^{+0.3}_{-0.6}$	<2.2
	$f_{\rm cov}$	$0.52^{+0.24}_{-0.26}$	$0.46^{+0.25}_{-0.23}$	$0.58^{+0.14}_{-0.22}$	$0.93^{+0.04}_{-0.08}$	$0.61^{+0.20}_{-0.16}$	$0.44^{+0.24}_{-0.34}$
Hot wind	$v_{\rm out}$ (c)	$0.22^{+0.03}_{-0.03}$	$0.17^{+0.02}_{-0.02}$	$0.17^{+0.01}_{-0.01}$	$0.11^{+0.02}_{-0.02}$	$0.11^{+0.01}_{-0.01}$	$0.10^{+0.05}_{-0.05}$
	$\theta_{\rm incl}$ (°)	$47.8^{+1.8}_{-1.4}$	$48.1^{+1.3}_{-1.3}$	$47.5^{+0.8}_{-0.7}$	<46.4	$46.8^{+0.5}_{-0.5}$	<46.9
Power law	Γ	$2.11^{+0.33}_{-0.23}$	$1.87^{+0.33}_{-0.26}$	$2.11^{+0.18}_{-0.16}$	$2.24^{+0.09}_{-0.09}$	$2.22^{+0.09}_{-0.08}$	$2.06^{+0.23}_{-0.22}$
	Norm. (10^{-4})	$3.0^{+2.7}_{-1.3}$	$1.6^{+1.6}_{-0.7}$	$2.3^{+1.2}_{-0.8}$	19^{+31}_{-11}	$4.5^{+5.3}_{-1.2}$	$2.2^{+1.7}_{-0.9}$
Fit statistics	χ^2_ν	79.99/58	76.06/101	133.33/148	124.24/141	172.42/177	101.09/112
	Null Prob.	0.029	0.97	0.80	0.84	0.58	0.76
	χ^2/ν	1.38	0.75	0.90	0.88	0.97	0.90
Saez & Chartas (2011)	χ^2/ν (extreme wind)	–	1.15	0.95	1.03	1.08	0.97

Table 5. Fitting parameters for all the *Suzaku* observations.

		OBS1	OBS2[a]	OBS3
Cold absorber	$N_{\rm H}$ (10^{22} cm^{-2})	$7.4^{+1.9}_{-1.4}$	$5.6^{+1.6}_{-1.9}$	$5.3^{+1.5}_{-1.7}$
Cool clump	$v_{\rm out}$ (c)	Tied to hot wind		
	$N_{\rm H}$ (10^{22} cm^{-2})	191^{+89}_{-79}	92^{+54}_{-40}	102^{+258}_{-56}
	$\log \xi$	<3.0	<2.4	$1.9^{+2.4}_{-2.3}$
	$f_{\rm cov}$	$0.81^{+0.11}_{-0.13}$	$0.59^{+0.18}_{-0.36}$	$0.57^{+0.08}_{-0.39}$
Hot wind	$v_{\rm out}$ (c)	$0.12^{+0.07}_{-0.06}$	$0.18^{+0.05}_{-0.04}$	$0.14^{+0.03}_{-0.03}$
	$\theta_{\rm incl}$ (°)	<46.5	<47.2	<46.7
Power law	Γ	$2.28^{+0.20}_{-0.16}$	$2.17^{+0.25}_{-0.26}$	$2.17^{+0.21}_{-0.31}$
	Norm. (10^{-4})	$6.8^{+8.9}_{-4.0}$	$2.8^{+2.5}_{-1.5}$	$2.7^{+1.7}_{-1.4}$
Fit statistics	χ^2_ν	125.02/130	130.60/124	161.75/142
	Null Prob.	0.61	0.32	0.12
	χ^2/ν	0.96	1.05	1.14

Note. [a]Data points of FI between 1.75 and 1.95 keV are ignored as in Saez et al. (2009).

4.2 Application to all *XMM–Newton*, *Chandra* and *Suzaku* data

We use the model derived above for Epoch 1 to fit all the data observed by *XMM–Newton*, *Chandra* and *Suzaku*. The velocity of the partially ionized absorber is tied to that of the hot wind since they are consistent in Epoch 1 spectrum. The best-fitting parameters for all the Epochs are listed in Tables 4 and 5, and the spectra and models are shown in Fig. 4. Magenta dashed lines indicate the best-fitting energies of the hot wind absorption lines for Epoch 1, where the absorption lines are most clearly detected. It is obvious that the line energies of the hot wind decrease over time. In the observations in 2001 and 2002 (Epoch 0–2), the absorption lines are the same or higher energies than those of Epoch 1, while in the observations after 2006 (OBS1–3, Epoch 3–5) the line energies are lower than those of Epoch 1. Also obviously, the depths of the absorption lines decrease in the later observations.

The column density of the cold absorber is fully consistent with constant. This is different from the previous study (Chartas et al. 2009) due to a significant improvement of the contamination models of *Chandra*. The old CALDB they used for Epoch 5 underestimates effects of the contamination (G. Chartas, private communication). The intrinsic continuum is also mainly consistent with being constant except for Epoch 3, which has a much higher intrinsic power-law flux. We think that this is an artefact as the observed high-energy flux does not show such large variability as discussed in Section 3.2. Instead, this is probably an artefact of our approximate model for the cool clump absorption as the column density of the partial coverer has also increased dramatically. Electron scattering from the clumps, which is currently modelled by CABS, strongly depends on the geometry. CABS only considers photons scattering out of our line of sight, but photons scattering into our line of sight could be important if the solid angle of the wind is not negligible. We demonstrate this by refitting the spectrum in Epoch 3 without the CABS component. This gives a smaller power-law normalization of $2.4^{+0.5}_{-0.4} \times 10^{-4}$ and a smaller covering factor of $0.44^{+0.07}_{-0.08}$, both of which are similar to the other observations. The other parameters are consistent within 90 per cent uncertainties with comparable fit statistics of $\chi^2_\nu = 124.0/141$.

The partially ionized absorber is moderately ionized ($\log \xi \sim 2$) in all the observations. It is less ionized than the hot wind, whose ionization parameter is typically $\log \xi \sim 5$. It produces absorption edges at energies lower than those of the H- and He-like iron in the hot wind, and distorts the continuum spectral shape. The continuum shape is strongly affected by covering factor and column density as well as the ionization parameter. Due to this model component, the intrinsic power-law continuum is steeper than in Chartas et al. (2009). On average, the photon index is $\Gamma \sim 2.2$, similar to that measured directly in the high-energy spectra (Section 3.2). This is slightly smaller than the $\Gamma = 2.5$ assumed to derive the ionization state in our disc wind model, but this only makes a 10–20 per cent difference in ionization parameter $\log \xi$. This effect is much smaller than the factor 10 uncertainty on ionization parameter which comes from the uncertainty in intrinsic luminosity due to the lens magnification.

The hot wind velocity clearly decreases from $\sim 0.2c$ to $\sim 0.1c$ during all the observation Epochs, as shown in the top panel of Fig. 5. This is not an artefact of the correlated change in inclination angle from $\sim 48°$ to $\sim 46°$ (lower panel of Fig. 5) as this corresponds to $\Delta v \simeq 0.004c$, which is much smaller than the decrease in the outflow velocity (Fig. 2). The decreasing angle is instead a consequence of a decreasing column density of the hot wind.

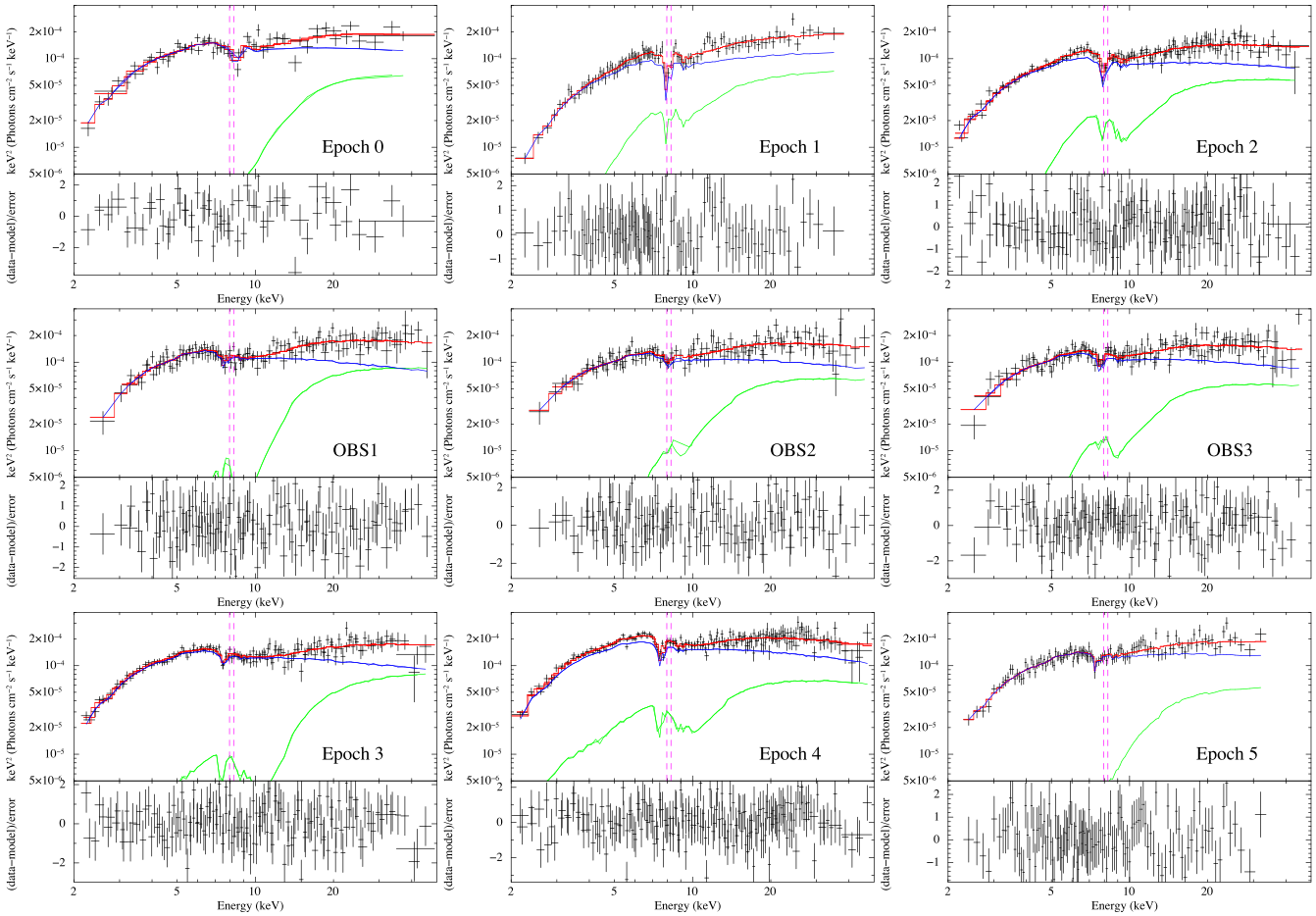

Figure 4. Observed spectra and best-fitting models for all Epochs. The absorbed component, unabsorbed component and sum of these components are plotted in green, blue and red, respectively. Magenta dashed lines indicate the best-fitting energies of the blueshifted Fe XXV/Fe XXVI absorption lines seen in Epoch 1. It is clear that the velocity of these systems is decreasing over time, as is their equivalent width.

5 DISCUSSION

5.1 Velocity of the wind

These data were previously fit by Chartas et al. (2009) and Saez & Chartas (2011). Our results agree fairly well in terms of the velocity of what we call the hot wind component and they call the slow wind (the component that produces the obvious absorption line in most of the spectra). However, they differ dramatically on how to interpret the rest of the complex absorption at higher energies. In our model, there is additional curvature from the edge structure from a partial covering, less ionized component, which we assume is outflowing at the same velocity as our hot wind as seen in the classic wind source PDS 456 (Matzeu et al. 2016). Instead, in Saez & Chartas (2011), this broad absorption feature is again fit by an iron resonance absorption line, so the observed width of the absorption requires a large range of velocities in the line of sight in this second wind component. The fastest material typically reaches speeds of 0.65–0.7c except in Epoch 1, where they only require 0.4c (their fast wind component). Thus, in their model there is material that is typically much faster than can be explained by any radiatively driven wind, whereas in ours this is not required.

The key question is then which wind model better matches the physical situation in this source. All models are only approximations to a more complex reality, but it is clearly useful to ask which one describes the data better. Our data have different numbers of points due to differences in extraction and grouping, so we include the reduced χ^2/ν for the Saez & Chartas (2011) model fits for Epoch 1–5 at the bottom of Table 4. Our fits all have lower χ^2_ν, despite there only being five free parameters to describe our complex wind (velocity, angle that controls the column density and velocity width of the hot wind, and then the cooler wind column, ionization state and covering fraction), compared to seven in their model (each wind has column density, and minimum and maximum outflow velocity, and then both winds are assumed to have the same ionization state).

The data clearly show that there are two absorption features. All models agree that the lower energy feature is mainly a resonance absorption iron line from material outflowing at 0.1–0.2c. This has enough energy to impact the host galaxy and is clear evidence for AGN feedback. The higher energy feature is more controversial. In our model, it is produced by the complex edge feature from the less ionized, partial covering material outflowing at the same velocity. These velocities are high but can be produced by radiation driving on a wind launched from inner disc. In the Saez & Chartas (2011) model, it is instead produced by a highly broadened absorption line that requires extreme velocities. Not only does our model gives better fit, but we note that the classic wind source, PDS 456 requires such partially ionized material that partially covers the source (Reeves et al. 2009; Hagino et al. 2015) and which is outflowing along with the material producing the resonance line

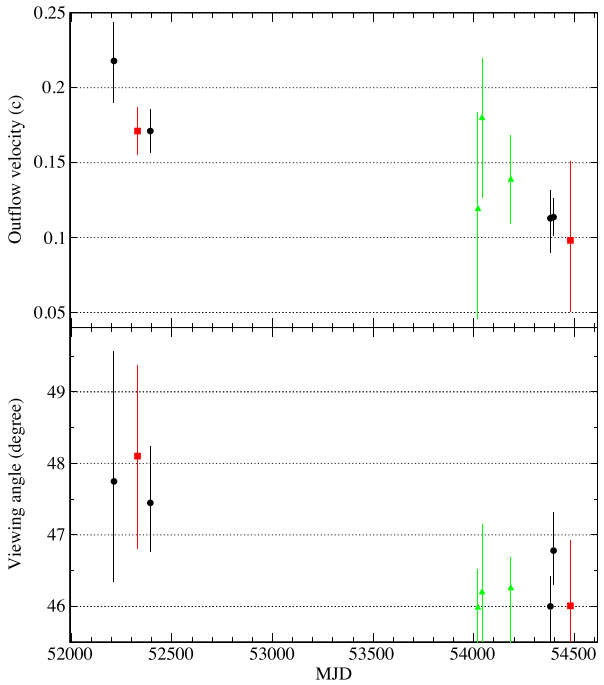

Figure 5. Outflow velocity and viewing angle of each observation (*XMM–Newton*: black circles, *Chandra*: red squares, *Suzaku*: green triangles) plotted as a function of MJD. Error bars correspond to 90 per cent confidence level.

(Matzeu et al. 2016). This supports our interpretation, but we need data from APM 08279+5255 which is of similar quality to that of PDS 456 in order to unambiguously distinguish between our model and the extreme wind.

5.2 Broadband SED and quasar parameters

The broad-band SED of the quasar is very important to understand the acceleration mechanisms of the wind. Strong UV radiation easily launches a wind by radiation pressure on UV line transitions, while strong X-rays suppress it. Hence, an SED that is UV bright and X-ray weak is clearly consistent with UV line driving, while one that has strong X-ray flux is less favourable.

We plot the broad-band SED from *Spitzer* (Soifer et al. 2004), *AKARI* (Oyabu et al. 2009), *2.5-m Isaac Newton Telescope* (*INT*; Benn et al. 2002) and *Chandra* (Epoch1) data. The optical continuum underneath the Hα line shows a clear disc spectrum, so we use this to constrain the mass accretion rate through the outer accretion disc via the OPTXAGNF model (Done et al. 2012). This includes phenomenological modelling of the soft X-ray excess and high-energy corona emission, assuming that these are energetically powered by the same mass accretion rate as required for the outer disc. This implies a transition radius, $R_{\rm cor}$, within which the energy released by gravity is dissipated in these X-ray components rather than the standard disc. We first fix the black hole mass to $M_{\rm BH} = 1.00^{+0.17}_{-0.13} \times 10^{10}$ M$_\odot$ and a magnification factor of $\mu \lesssim 8$ as obtained by reverberation mapping of the Si IV and C IV emission lines (Saturni et al. 2016). We set the normalization of OPTXAGNF as equal to the magnification factor, fix the soft X-ray excess to typical values of $kT_e = 0.2$ keV and an optical depth of $\tau = 15$, fix the fraction of coronal emission to a typical value of $f_{\rm pl} = 0.3$, with spectral index $\Gamma = 2.2$ as observed. We find that the broad-band SED is well reproduced by a model with $\mu = 6$, $M_{\rm BH} = 1 \times 10^{10}$ M$_\odot$,

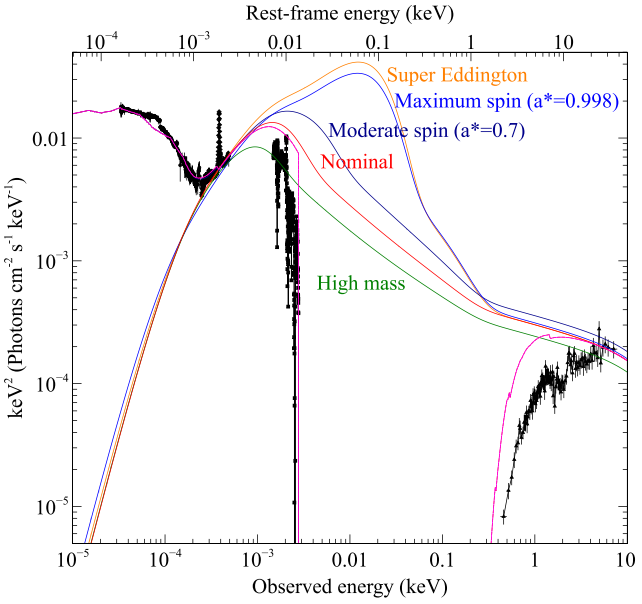

Figure 6. Broadband SED of APM 08279+5255 from *Spitzer* (black circles: Soifer et al. 2004), *AKARI* (diamonds: Oyabu et al. 2009), *INT* (squares: Benn et al. 2002) and *Chandra* (triangles: Chartas et al. 2002). The red line is model for the accretion flow with nominal parameters ($M_{\rm BH} = 10^{10}$ M$_\odot$, $L_{\rm bol}/L_{\rm Edd} = 1$, $\mu = 6$), while the magenta line shows reddening/absorption from our Galaxy and absorption by the constant gas column of 5×10^{22} cm^{-2} seen in the X-ray data. We also include template model to fit the IR torus emission in order to determine its luminosity. The green line shows the upper limit to black hole mass for zero spin of $M_{\rm BH} = 2 \times 10^{10}$ M$_\odot$ ($L_{\rm bol}/L_{\rm Edd} = 0.5$, $\mu = 4$), as the optical/UV continuum has to be at least as strong as the observed *INT* flux (it can be higher as there is substantial Lyman α forest absorption). Both Nominal and high-mass models underpredict the observed IR flux, requiring that the SED peaks at higher energies. The dark blue line shows a solution with moderate black hole spin $a^* = 0.7$ ($M_{\rm BH} = 10^{10}$ M$_\odot$, $L_{\rm bol}/L_{\rm Edd} = 1$ and $\mu = 8$), while the blue line shows maximum black hole spin $a^* = 0.998$ ($M_{\rm BH} = 10^{10}$ M$_\odot$, $L_{\rm bol}/L_{\rm Edd} = 1$ and $\mu = 15$). The orange line shows instead the lower limit of black hole mass $M_{\rm BH} = 4 \times 10^9$ M$_\odot$ and high Eddington ratio of $L_{\rm bol}/L_{\rm Edd} = 25$ ($a^* = 0$ and $\mu = 2$). Full parameters for these are listed in Table 6.

$L_{\rm bol}/L_{\rm Edd} = 1$ and $r_{\rm corona} = 25 r_{\rm g}$. This coronal radius is a typical value for AGN with an accretion rate close to Eddington (Jin et al. 2012). This intrinsic spectrum is shown by the red line marked 'Nominal' in Fig. 6, whereas the magenta line in this figure includes the effect of absorption in our Galactic cold absorber with $N_{\rm H} = 5 \times 10^{22}$ cm^{-2} introduced to explain the strong X-ray continuum absorption. We only include dust reddening from our Galaxy because the very high column density in the cold absorber would strongly suppress the optical flux down to much lower level than the observed flux. This means that the cold absorber is not dusty so it cannot be associated with the torus or other material further out in the host galaxy.

The magenta line also includes a torus template by Silva, Maiolino & Granato (2004) to reproduce the mid-IR data observed by *Spitzer*. We use this torus template to estimate the power of dust emission, and its ratio to the accretion power. This ratio must be less than unity as the torus is powered by reprocessing of the illuminating AGN flux. However, Table 6 shows that the torus is more luminous than the total accretion power in the Nominal SED model. This discrepancy is only made worse if the magnification is

Table 6. Parameters for the solutions to explain the broad-band SED.

	$M_{\rm BH}$ ($M_\odot$)	a^*	$\dot{m}$	μ	$\frac{L_{\rm dust}}{L_{\rm AGN}}$
Nominal (red)	10^{10}	0	1	6	1.35
High mass (green)	2×10^{10}	0	0.5	4	2.03
Moderate spin (dark blue)	10^{10}	0.7	1	8	0.99
Maximum spin (blue)	10^{10}	0.998	1	15	0.48
Super-Eddington (orange)	4×10^9	0	25	2	0.40

different between the IR and the nuclear region, as more extended IR will have smaller magnification.

We investigate the effect of changing the model parameters. First, we investigate what happens with a larger black hole mass, as reverberation mapping is clearly very difficult with the UV lines. A higher black hole mass would give a lower temperature of the accretion disc, but there is a limit to how low this can go while still fitting the *INT* optical data. The model flux cannot be lower than this data, but can be higher as there is substantial Lyman α forest absorption that additionally suppresses the optical/UV spectrum. We find that this requirement means that there is an upper limit of the black hole mass for zero spin of $M_{\rm BH} \sim 2 \times 10^{10}\,{\rm M}_\odot$, which is plotted in green in Fig. 6, called 'high mass'. In this parameter set, we use a lower limit of the Eddington ratio ($L_{\rm bol}/L_{\rm Edd} = 0.5$) determined by the correlation of photon index and Eddington ratio (see Section 3.2) since the lower accretion rate decreases the disc temperature. The magnification factor is $\mu = 4$, and the corona radius is $r_{\rm corona} = 40 r_{\rm g}$, which is reasonable for a half Eddington accretion, but now the mismatch with the IR emission is even worse (see Table 6).

A possible solution to reproduce both the accretion flow emission and the torus reprocessing is to shift the peak of the quasar radiation to higher energies, into the unobservable far-UV. The maximum disc temperature $T_{\rm max}$ follows a proportional relation

$$T_{\rm max} \propto \dot{m}^{1/4} {M_{\rm BH}}^{-1/4} {r_{\rm ISCO}}^{-3/4} \quad (1)$$

so is higher for a larger Eddington ratio $\dot{m}(\equiv L_{\rm bol}/L_{\rm Edd})$, a smaller black hole mass $M_{\rm BH}$ or a smaller disc inner radius $r_{\rm ISCO}$ (which depends on the black hole spin a^*). We have to simultaneously reproduce the observed optical flux $F_{\rm opt} \propto \mu(M_{\rm BH}\dot{M}_{\rm acc})^{2/3}$ (Davis & Laor 2011), with the additional relation from the bolometric luminosity $L_{\rm bol} \propto \dot{m} M_{\rm BH} \propto \eta \dot{M}_{\rm acc}$, where η is the spin-dependent efficiency of the energy conversion. This requires

$$\dot{m} \propto \eta \mu^{-3/2} {M_{\rm BH}}^{-2}. \quad (2)$$

The solutions are limited by ranges of the parameters. The lower limit of the black hole mass can be estimated by a comparison of the width of the broad line with PDS 456. PDS 456 ($M_{\rm BH} = 1$–$2 \times 10^9\,{\rm M}_\odot$) has an H$\beta$ line width of $3974 \pm 764\,{\rm km\,s^{-1}}$ (Torres et al. 1997), a factor 2 smaller than an Hα line width of $7721\,{\rm km\,s^{-1}}$ in APM 08279+5255 (Oyabu et al. 2009). The black hole mass depends on the velocity and radius of the broad line region, with $M_{\rm BH} \propto R v^2$. Hence, the black hole mass of APM 08279+5255 must be larger than $4 \times 10^9\,{\rm M}_\odot$ even in the unlikely case that R is the same. While the upper limit of the magnification factor is estimated by the reverberation mapping (Saturni et al. 2016), the lower limit is not. Here, we simply set a lower limit to be $\mu = 2$ since no magnification $\mu = 1$ seems to be unlikely for such a high-luminosity object. We consider two possible upper limits for the spin parameter in this source. We first assume that the spin is less than $a^* \sim 0.7$, as might perhaps be appropriate if this source is radio-quiet, as high spin may always result in a powerful radio jet (Maraschi et al. 2012; Done & Jin 2016).

A solution with a moderate black hole spin of $a^* = 0.7$ at Eddington is plotted in dark blue in Fig. 6. Higher spin gives higher efficiency so higher luminosity for a given mass accretion rate through the outer disc. The magnification factor must be larger to compensate the increase of η following equation (2). We find that setting the magnification factor at its upper limit ($\mu = 8$) can reproduce the observed spectra. In this case, the ratio of reprocessed IR to total accretion power is ~99 per cent, which just barely avoids violating energy conservation.

We also consider a maximally spinning black hole (spin parameter of $a^* = 0.998$). This requires a large magnification factor $\mu = 15$ for $L_{\rm bol}/L_{\rm Edd} = 1$ but the torus luminosity fraction is now a more acceptable value of 48 per cent. While highly relativistic jets are not well understood, it is clear that spin plays at least some role. APM 08279+5255 does have radio emission and its luminosity does put it into the FRII category so it could indeed have a misaligned, highly powerful radio jet, but some (perhaps all) of this radio emission is powered by the strong star formation (Riechers et al. 2009). The high-resolution radio images show no sign of a double radio structure (Riechers et al. 2009), but these could be suppressed by being on scales that are outside of the lensing magnification and/or the source could be young, like the GHz-peaked AGN (Bruni et al. 2015).

The other possible solutions are higher accretion rate or/and lower black hole mass. A lower limit of black hole mass $M_{\rm BH} = 4 \times 10^9\,{\rm M}_\odot$ corresponds to $\dot{m} = 6.25$ by equation (2) if the magnification factor and the spin are unchanged. By using a lower limit of magnification factor $\mu = 2$, the Eddington ratio becomes as high as $\dot{m} = 25$. This magnification factor is slightly lower than that calculated from equation (2) because the relation $F_{\rm opt} \propto \mu(M_{\rm BH}\dot{M}_{\rm acc})^{2/3}$ is only valid at energies below the disc peak. The model spectra with these parameters are plotted in orange in Fig. 6, again giving a more acceptable luminosity fraction of the torus compared to the accretion power of 40 per cent.

Exactly where the SED peaks is also important for the launch mechanism of the wind. According to the discussion in Laor & Davis (2014), the UV-line-driven disc wind is efficiently accelerated by radiation with an effective temperature of ~30 000–50 000 K. This corresponds to a peak in νf_ν at ~0.01 keV. Both nominal and high-mass models peak at energies that are somewhat below this, so may not have enough UV for efficient line driving. However, these are the two models that were ruled out by energy conservation as they cannot power the observed IR radiation. Instead, the higher spin and super-Eddington models all have copious UV photons at ~0.01 keV, yet are also X-ray weak. Thus, the broad-band SED of APM 08279+5255 is like that of PDS 456, in being UV bright and X-ray weak, as required for efficient UV line driving.

5.3 Relation with the broad UV absorption

Spectral fitting with our hot wind with cool clumps model revealed that the outflow velocity decreases from ~0.2c to ~0.1c while the viewing angle (which traces the column density) of the wind also decreases from ~48° to ~46° during 6 yr between 2001 October 30 and 2008 January 14. This was not discussed in previous work because their analysis concentrated on the putative faster components of the wind.

Similar trends are observed in the outflows seen in UV band. Trevese et al. (2013) investigated the long-term variability of the absorption line profiles from 1998 to 2012, which spans the time of

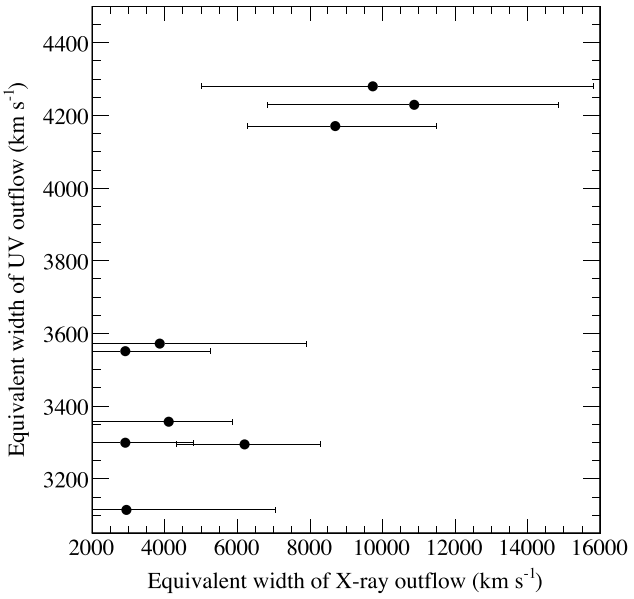

Figure 7. The equivalent width of the UV outflows (co-added BAL and blue and red NALs) versus that of X-ray outflow. The decrease in X-ray equivalent width with time seen from our data (modelled as a change in viewing angle: lower panel of Fig. 5) is correlated with the decrease in the UV absorption seen by Trevese et al. (2013).

the X-ray observations. They separate the C IV absorption systems into four components, two which are blends of narrower lines (blue NAL and red NAL) and two which are intrinsically broad (BAL1 and BAL2). They found that the equivalent widths of all these UV features decrease together, so we co-add their equivalent widths to measure the total UV absorption. We estimate this at the time of the X-ray observations by a linear interpolation.

The X-ray equivalent width was evaluated from the viewing angle of our wind model (see Fig. 2), and converted into units of velocity km s^{-1} for consistency with the values of the UV outflows. Fig. 7 shows that the X-ray and UV absorption equivalent widths decrease together. This would be easy to explain if the SED has changed as then both winds would be responding to the same change in ionizing flux. However, Trevese et al. (2013) shows the *R*-band magnitude is stable within less than ∼10 per cent, and the X-ray intrinsic luminosity is also stable to within ∼50 per cent as shown in Section 3.2.

Instead, we could explain the correlated change if both absorbers are a part of the same structure. However, this seems most unlikely as they have very different velocities, 0.1–0.2c for the X-ray absorber and 0.04c for the UV, and very different velocity behaviour as a function of time. The X-ray absorber slows (see Table 4) but UV absorption systems remain at a fixed velocity.

It is possible that the X-ray wind acts as a shield for the UV wind (Murray & Chiang 1998). A decreasing column density of the X-ray wind would then increase irradiation of the UV wind, decreasing the C IV ion fraction. We estimate the time-scale on which the column density can change considering the large black hole mass and the high redshift of this source. The wind in APM 08279+5255 changes over 6 yr, which corresponds to 1 yr at the quasar's rest frame. This corresponds to a size scale of $\sim 100 r_{\rm g}$ assuming a mass of 10^{10} M$_\odot$ using a velocity of ∼0.1–0.2c. This scale is very similar to the inhomogeneity of the UV-line-driven disc wind seen in the hydrodynamic simulations (e.g. Proga et al. 2000). In the archetypal wind source PDS 456, the time-scale for this kind of change is much smaller. Since the black hole mass is ∼10 times larger, and time dilation by the redshift is ∼5 times larger than PDS 456, the typical time-scale in PDS 456 is ∼50 times smaller than APM 08279+5255. It means that the 6 yr decrease of the mass outflow rate in this source corresponds to a variability in ∼1.5 months in PDS 456.

5.4 The other gravitationally lensed quasars

A few gravitationally lensed quasars at high redshift have features around iron which have been modelled by extremely smeared reflection (Reis et al. 2014; Reynolds et al. 2014; Walton et al. 2015; Lanzuisi et al. 2016). These fits result in a high black hole spin of $a^* \sim 0.7$–0.9, which has important implications for black hole evolution across cosmic time. However, the iron-K spectral feature in these sources might be interpreted as being instead from a wind, similar to that seen in APM 08279+5255. Lanzuisi et al. (2016) show that partially ionized, partial covering matches the spectral features in the lensed redshift ∼2 quasar PG 1247+267 as well (or even better than) relativistic reflection models. As shown in Hagino et al. (2016), the wind absorption with a larger viewing angle produces a similar spectral feature to the extremely smeared relativistic reflection. As an example, the iron-K feature in the most extreme relativistic reflection source 1H 0707-495 is successfully explained by the wind model.

6 CONCLUSIONS

We have successfully explained the observed X-ray spectra of APM 08279+5255 by a hot disc wind and a cool partially covering absorber with a non-extreme wind velocity ∼0.1–0.2c. This model does not require the extremely fast disc wind of previous work because the higher energy absorption feature is matched by the additional curvature from the edge structure in the cooler material rather than by an extremely broadened absorption line. This means that the wind in our interpretation can be powered by radiation driving especially as the source is UV bright, X-ray weak and close to (or exceeding) the Eddington limit. However, to unambiguously distinguish our model and the extreme wind model requires much better data than currently available.

We show that the X-ray absorber has decreased in both velocity and equivalent width over a timespan of 6 yr, correlated with a decrease in the equivalent width (but not velocity) of the ∼0.04c C IV UV broad absorption line. This correlation is not driven by the observed illuminating flux as this remains constant. Instead, it may indicate that the X-ray wind acts as a shield for the BAL.

ACKNOWLEDGEMENTS

The authors are grateful to Martin Hardcastle for discussions on the radio emission from APM 08279+5255. KH was supported by the Japan Society for the Promotion of Science (JSPS) Research Fellowship for Young Scientists. This work was supported by JSPS KAKENHI grant numbers 15H06897 and 24105007. CD acknowledges STFC funding under grant ST/L00075X/1 and a JSPS long-term fellowship.

REFERENCES

Begelman M. C., McKee C. F., Shields G. A., 1983, ApJ, 271, 70
Benn C., Vigotti M., Pedani M., Holt J., Mack K.-H., Curran R., Sánchez S., 2002, MNRAS, 329, 221

Bruni G., Mack K.-H., Montenegro-Montes F. M., Brienza M., González-Serrano J. I., 2015, A&A, 582, A9
Castor J. I., Abbott D. C., Klein R. I., 1975, ApJ, 195, 157
Chartas G., Brandt W. N., Gallagher S. C., Garmire G. P., 2002, ApJ, 579, 169
Chartas G., Saez C., Brandt W. N., Giustini M., Garmire G. P., 2009, ApJ, 706, 644
Davis S. W., Laor A., 2011, ApJ, 728, 98
Done C., Jin C., 2016, MNRAS, 460, 1716
Done C., Davis S. W., Jin C., Blaes O., Ward M., 2012, MNRAS, 420, 1848
Egami E., Neugebauer G., Soifer B. T., Matthews K., Ressler M., Becklin E. E., Murphy T. W. Jr., Dale D. A., 2000, ApJ, 535, 561
Elvis M., 2000, ApJ, 545, 63
Fukumura K., Kazanas D., Contopoulos I., Behar E., 2010, ApJ, 723, L228
Gofford J., Reeves J. N., Tombesi F., Braito V., Turner T. J., Miller L., Cappi M., 2013, MNRAS, 430, 60
Grupe D., Komossa S., Leighly K. M., Page K. L., 2010, ApJS, 187, 64
Hagino K., Odaka H., Done C., Gandhi P., Watanabe S., Sako M., Takahashi T., 2015, MNRAS, 446, 663
Hagino K., Odaka H., Done C., Tomaru R., Watanabe S., Takahashi T., 2016, MNRAS, 461, 3954
Higginbottom N., Proga D., Knigge C., Long K. S., Matthews J. H., Sim S. A., 2014, ApJ, 789, 19
Jin C., Ward M., Done C., Gelbord J., 2012, MNRAS, 420, 1825
Kallman T. R., Palmeri P., Bautista M. A., Mendoza C., Krolik J. H., 2004, ApJS, 155, 675
Kara E. et al., 2015, MNRAS, 449, 234
King A. R., 2010, MNRAS, 402, 1516
Knigge C., Woods J. A., Drew J. E., 1995, MNRAS, 273, 225
Krips M., Peck A. B., Sakamoto K., Petitpas G. B., Wilner D. J., Matsushita S., Iono D., 2007, ApJ, 671, L5
Krolik J. H., McKee C. F., Tarter C. B., 1981, ApJ, 249, 422
Laha S., Guainazzi M., Dewangan G. C., Chakravorty S., Kembhavi A. K., 2014, MNRAS, 441, 2613
Lanzuisi G. et al., 2016, A&A, 590, A77
Laor A., Davis S. W., 2014, MNRAS, 438, 3024
Lewis G. F., Carilli C., Papadopoulos P., Ivison R. J., 2002, MNRAS, 330, L15
Maraschi L., Colpi M., Ghisellini G., Perego A., Tavecchio F., 2012, J. Phys. Conf. Ser., 355, 012016
Matzeu G. A., Reeves J. N., Nardini E., Braito V., Costa M. T., Tombesi F., Gofford J., 2016, MNRAS, 458, 1311
Murray N., Chiang J., 1998, ApJ, 494, 125
Nardini E. et al., 2015, Science, 347, 860
Nomura M., Ohsuga K., Wada K., Susa H., Misawa T., 2013, PASJ, 65, 40
Nomura M., Ohsuga K., Takahashi H. R., Wada K., Yoshida T., 2016, PASJ, 68, 16
Odaka H., Aharonian F., Watanabe S., Tanaka Y., Khangulyan D., Takahashi T., 2011, ApJ, 740, 103
Oyabu S., Kawara K., Tsuzuki Y., Matsuoka Y., Sameshima H., Asami N., Ohyama Y., 2009, ApJ, 697, 452
Pounds K. A., Reeves J. N., King A. R., Page K. L., O'Brien P. T., Turner M. J. L., 2003a, MNRAS, 345, 705
Pounds K. A., King A. R., Page K. L., O'Brien P. T., 2003b, MNRAS, 346, 1025
Proga D., Kallman T. R., 2004, ApJ, 616, 688
Proga D., Stone J. M., Kallman T. R., 2000, ApJ, 543, 686
Reeves J. N., O'Brien P. T., Ward M. J., 2003, ApJ, 593, L65
Reeves J. N. et al., 2009, ApJ, 701, 493
Reeves J. N. et al., 2014, ApJ, 780, 45
Reis R. C., Reynolds M. T., Miller J. M., Walton D. J., 2014, Nature, 507, 207
Reynolds M. T., Walton D. J., Miller J. M., Reis R. C., 2014, ApJ, 792, L19
Riechers D. A., Walter F., Carilli C. L., Lewis G. F., 2009, ApJ, 690, 463
Risaliti G., Elvis M., 2010, A&A, 516, A89
Saez C., Chartas G., 2011, ApJ, 737, 91
Saez C., Chartas G., Brandt W. N., 2009, ApJ, 697, 194
Saturni F. G., Trevese D., Vagnetti F., Perna M., Dadina M., 2016, A&A, 587, A43
Shemmer O., Brandt W. N., Netzer H., Maiolino R., Kaspi S., 2006, ApJ, 646, L29
Shemmer O., Brandt W. N., Netzer H., Maiolino R., Kaspi S., 2008, ApJ, 682, 81
Shlosman I., Vitello P., 1993, ApJ, 409, 372
Silva L., Maiolino R., Granato G. L., 2004, MNRAS, 355, 973
Sim S. A., Long K. S., Miller L., Turner T. J., 2008, MNRAS, 388, 611
Sim S. A., Miller L., Long K. S., Turner T. J., Reeves J. N., 2010a, MNRAS, 404, 1369
Sim S. A., Proga D., Miller L., Long K. S., Turner T. J., 2010b, MNRAS, 408, 1396
Soifer B. T. et al., 2004, ApJS, 154, 151
Solomon P., Vanden Bout P., 2005, ARA&A, 43, 677
Takahashi H. R., Ohsuga K., 2015, PASJ, 67, 60
Takeuchi S., Ohsuga K., Mineshige S., 2014, PASJ, 66, 48
Tombesi F., Cappi M., 2014, MNRAS, 443, L104
Tombesi F., Cappi M., Reeves J. N., Palumbo G. G. C., Yaqoob T., Braito V., Dadina M., 2010, A&A, 521, A57
Torres C. A. O., Quast G. R., Coziol R., Jablonski F., de la Reza R., Lépine J. R. D., Gregório-Hetem J., 1997, ApJ, 488, L19
Trevese D., Saturni F. G., Vagnetti F., Perna M., Paris D., Turriziani S., 2013, A&A, 557, A91
Walton D. J., Reynolds M. T., Miller J. M., Reis R. C., Stern D., Harrison F. A., 2015, ApJ, 805, 161
Wang J.-M., Watarai K.-Y., Mineshige S., 2004, ApJ, 607, L107
Watanabe S. et al., 2006, ApJ, 651, 421
Weiß A., Downes D., Neri R., Walter F., Henkel C., Wilner D. J., Wagg J., Wiklind T., 2007, A&A, 467, 955

This paper has been typeset from a TEX/LATEX file prepared by the author.